University of Bath

Alternative formats
If you require this document in an alternative format, please contact:
openaccess@bath.ac.uk

Metallic Conductivity in a Two-Dimensional Cobalt Dithiolene Metal-Organic Framework

Andrew J. Clough,[‡] Jonathan M. Skelton,[†] Courtney A. Downes,[‡] Ashley de la Rosa,[‡] Joseph W. Yoo,[‡] Aron Walsh,[†] Brent C. Melot,[‡*] and Smaranda C. Marinescu[‡*]

[‡]Department of Chemistry, University of Southern California (USC), Los Angeles, CA 90089, USA

[†]Department of Materials, Imperial College London, London, UK

Supporting Information Placeholder

ABSTRACT: Two-dimensional (2D) metal-organic frameworks (MOFs) have received a great deal of attention due to their relatively high charge carrier mobility and low resistivity. Here we report on the temperature-dependent charge transport properties of a 2D cobalt 2,3,6,7,10,11-triphenylenehexathiolate framework. Variable temperature resistivity studies reveal a transition from a semiconducting to a metallic phase with decreasing temperature, which is unprecedented in MOFs. We find this transition to be highly dependent on the film thickness and the amount of solvent trapped in the pores, with density functional theory (DFT) calculations of the electronic-structure supporting the complex metallic conductivity of the material. These results identify the first experimentally observed MOF that exhibits band-like metallic conductivity.

INTRODUCTION

The development of inexpensive yet highly efficient catalysts for solar-to-fuel energy conversion is vital for mitigating the adverse effects that hydrocarbon fuels have on the environment.[1] Immobilization of molecular catalytic units is an attractive strategy for bridging the gap between homogeneous and heterogeneous electrocatalysis for solar-to-fuel applications.[2] This approach retains the desirable properties of molecular systems, like well-defined chemistries and clear design principles, while also taking advantage of the robust efficiency of heterogeneous catalysts.[2] Metal-organic frameworks, a rapidly expanding class of nanoporous coordination polymers,[3] have attracted growing attention because they sit at the interface between molecules and extended solids, offering a mixture of high surface-to-volume ratio and site-isolation of catalytic units, all of which are indicators to systems with enhanced activities. Yet, the biggest challenge these materials face for designing new electrocatalysts is rooted in their ability to efficiently transport charge between the metals and their coordinating ligands.[4]

In this regard, 2D frameworks[5] have been shown to exhibit high charge-carrier mobility because of in-plane charge delocalization and extended π–conjugation within the sheets.[6] Recent studies have demonstrated that nickel or copper 2,3,6,7,10,11-hexaiminotriphenylene ($M_3(HITP)_2$, M = Ni, Cu) frameworks can exhibit thin film conductivities on the order of 40 S·cm^{-1} while copper benzenehexathiolate frameworks can be as high as 1580 S·cm^{-1}, which is one of

the highest conductivities reported for any coordination polymer.[7] Yet, the transport properties are usually the result from inadvertent doping of an intrinsic semiconductor that can be synthetically difficult to control rather than a truly metallic charge delocalization.

In a previous report, we showed that 2,3,6,7,10,11-triphenylenehexathiolate can be used to produce a periodic 2D network of cobalt dithiolene units as illustrated in Figure 1.[8] This phase displays remarkable activity for the electrocatalytic H_2 evolution from water,[8] and is one of the first examples of an electrocatalytically active MOF.[9] This motivated us to investigate the source of this high catalytic performance by characterizing its charge transport characteristics. Here, we report the first observation of a temperature-dependent transition in a MOF from a semiconducting to a metallic phase with decreasing temperature using a combination of thin film resistivity measurements and DFT calculations, with metallic conductivity persisting to temperatures as high as 225 K.
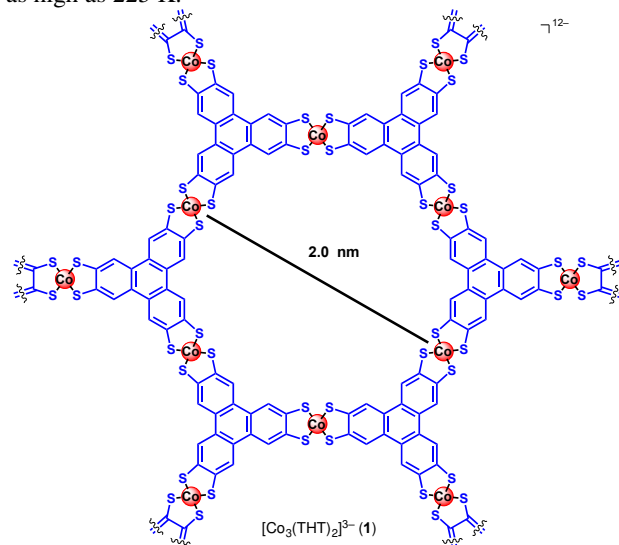
Figure 1. Framework of the 2D cobalt dithiolene framework $[Co_3(THT)_2]^{3-}$, **1**, studied here.

RESULTS AND DISCUSSION

Framework **1** was prepared using a slightly modified procedure from previous reports.[8] The material adopts a hexagonal 2D structure with long-range order in the *ab* plane as evidenced by the sharp Bragg reflections in the synchrotron X-ray diffraction pattern shown in Figure 2. The pattern ex-

hibits prominent peaks at 1.2°, 2.4°, 3.2°, and 4.2°, which correspond to a significant degree of coherence within the 2D sheets. The somewhat broader reflection at 7.2° corresponds to the [001] reflection, suggesting less coherence between the sheets as is common for layered materials.[10] Regardless, the experimental diffraction pattern is a close approximation to simulations from the Materials Studio suite of programs (Figure S1) using the idealized structure with layers that are stacked in perfect registry. The optimized structure is best described using P6/*mmm* as the space group with unit cell parameters of $a = b = 22.52$ Å and $c = 3.3$ Å (Figure 2).
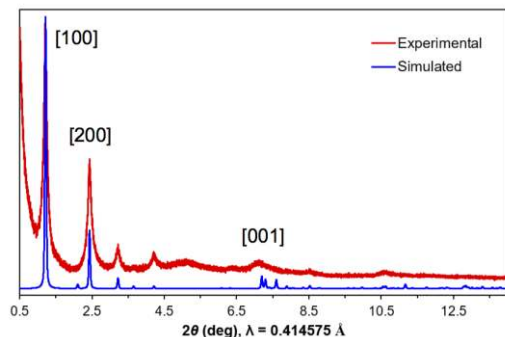

Figure 2. Experimental and simulated PXRD patterns of **1**.

Gas sorption isotherms performed on **1** reveal a Brunauer-Emmett-Teller (BET) surface area of 370 $m^2 g^{-1}$ (Figure S3), which is similar to that of the previously reported platinum analogue.[6f] Temperature-dependent susceptibility measurements show a response characteristic of localized moments. A fit of the high temperature magnetic susceptibility data (200K–300K) to the Curie-Weiss equation ($\chi = C/(T-\theta_{CW}) + \chi_0$) yields an effective paramagnetic moment, $\mu_{eff} = 1.55$ μ_B per formula unit, $\theta_{CW} = -34K$, and $\chi_0 = 3.57 \times 10^{-4}$ emu mol^{-1} Oe^{-1} (Figure S4). The positive temperature-independent term reflects a background paramagnetic signal that could result from the presence of some charge delocalization or more simply from second-order Zeeman effects.[11] The moment is slightly reduced from what is expected for an S = 1/2 state, which should show a theoretical moment of 1.87 μ_B. Such an underestimate is often ascribed to orbital quenching due to covalency, and indicates the presence of only one unpaired spin per formula unit. Given the presence of three square-planar cobalt ions per unit cell, this is consistent with two thirds of the Co adopting the trivalent state (S = 0) with one exhibiting a formal divalent (S = 1/2) state, which is significant since mixed oxidation states are often associated with charge delocalization.[12]

The temperature-dependent resistivity of **1** was measured using a four-point Van der Pauw geometry on a pressed pellet of **1** with a thickness of 0.24(2) mm. Graphitic carbon paint (Alfa Aesar) was used to create Ohmic contacts, as verified by the linear I-V trace shown in Figure S5. InGa eutectic and silver paint were also used to create Ohmic contacts and gave qualitatively similar results; however, the carbon paint was the best at maintaining physical contact over the entire temperature range of interest. At 300 K, the bulk resistivity was determined to be 0.720(7) kΩ-cm, corresponding to a conductivity of 1.4×10^{-3} S·cm^{-1}, which is in line with values reported for the platinum analogue.[6f] Given the highly anisotropic nature of the pressed pellet of **1**, this relatively low value is likely associated with the random

orientation of the powder and is likely exaggerated by grain-boundary scattering between the sheet-like particles.

An exponential rise in the resistivity of the pellet is seen between 300 K and 170 K, as would be expected for a semiconducting sample where transport is dominated by thermally populated carriers that must overcome a hopping barrier for conduction (Figure 3a).[13] An Arrhenius fit to the data suggests an activation energy on the order of 173 meV (Figure S6). More interestingly, a decrease in the resistivity is subsequently seen between 130 K and 50 K, suggesting a transition to a metallic phase where scattering of the carriers is dominated by lattice vibrations. The transition is fully reversible, with no signs of hysteresis as illustrated in Figure S7, suggesting it is second order in nature, unlike the metal-to-insulator transitions in materials like VO_2 that are associated with structural deformations.[14] To further confirm the absence of a coherent structural distortion, variable temperature synchrotron powder X-ray diffraction studies were performed between 300 and 100 K. As indicated in Figure S8–10, the only significant change to the diffraction patterns is a slight shift in the [001] reflection from 7.11° (300 K) to 7.15° (100 K), which corresponds to a 0.02 Å contraction of the interlayer spacing or a roughly 1% change.

To explore this transition further, films of **1** were deposited on glass supports with scanning electron microscopy (SEM) images indicating smooth surfaces and good coverage (Figures 3a insert and S11). The thicknesses of the films were determined using atomic force microscopy (AFM) and ranged from 0.1 and 0.2 μm (Figures S12–13) with the resistivity being measured in an identical fashion to the pellets described earlier (Figures 3 and S14–18). For films with a thickness of 0.20 μm, the resistivity at 300 K was 31 Ω-cm, corresponding to a conductivity of 3.2×10^{-2} S·cm^{-1}, which is a full order of magnitude higher than the conductivity of the pellet as expected when grain boundaries between the sheet-like particles are reduced. The temperature-dependent resistivity data of the films show a similar semiconductor-to-metal transition (Figure 3a). Interestingly, the transition temperature exhibits a strong correlation with film thickness, with thinner films displaying a higher temperature transition to a metallic state and thicker films remaining semiconducting to lower temperatures (Table S1).
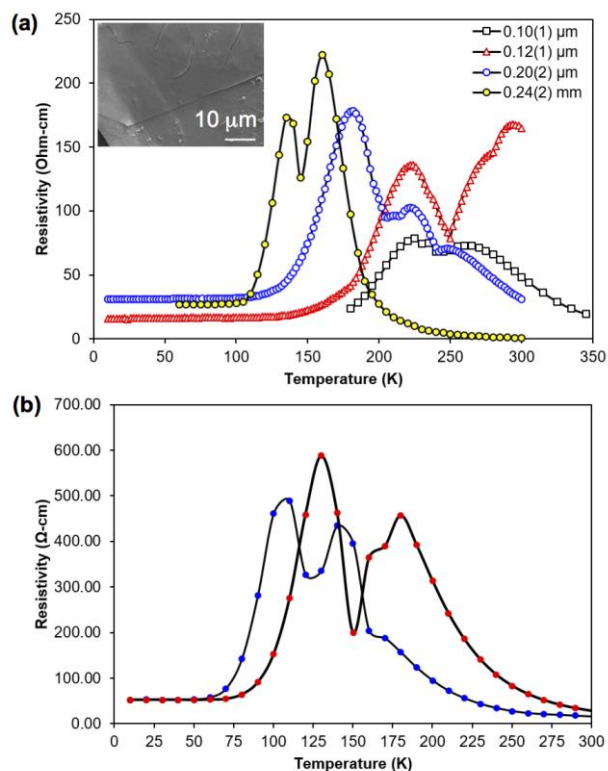
Figure 3. Variable-temperature resistivity data for (a) solid **1** pressed in a pellet of 0.24(2) mm thickness (yellow, scaled down 10^5 ×) and films of **1** with thicknesses of 0.10(1) (black), 0.12(1) (red), and 0.20(2) (blue) μm deposited on glass supports; or (b) films of **1** with thicknesses of 0.5(1) μm before (blue) and after (red) a two-hour exposure under vacuum at 90 °C. Insert (a): an SEM image of film **1**.

The nanoporous nature of MOFs is well-known to result in a significant amount of solvent being trapped within the channels.[3] To investigate if the presence of trapped solvent has an influence on the transition temperature, the variable temperature resistivity data of a film of 0.5(1) μm thickness was measured before and after a two-hour exposure under vacuum at 90 °C (Figures 3b, S19–20). These measurements clearly indicate that the films with less solvent display an increase in the metallic transition temperature from 105 to 130 K. XPS studies before and after the conductivity experiments show no significant changes suggesting that the films are not significantly altered by the thermal treatment (Figure S21).

On closer inspection of the transition, there are clearly two closely spaced maxima in the resistivity data. While unusual, this type of transition has been observed in glassy charge transfer salt κ-(BEDT-TTF)$_2$Cu[N(CN)$_2$]Br (where BEDT-TTF = bis-ethylenedithiotetrathiafulvalene).[15] In this instance, the authors ascribed the unusual temperature dependence to a strong contribution from lattice vibrations at higher temperatures in combination with highly anisotropic changes to their in-plane lattice parameters. Both of these effects are likely at play in **1** as the temperature-dependent synchrotron diffraction data shows a substantially more pronounced change to the inter-layer spacing compared to the distances within the sheets. Considering that the transitions in the resistivity are not reflected in the magnetic susceptibility, they are unlikely to be associated with an in-plane structural dis-

tortion, which should alter the coupling between the spins. Furthermore, the removal of solvent from the material would most likely result in a tighter packing of crystallites and more interfacial contact between the sheet-like particles. Thus, our experimental data suggests that changes in the vibrational modes, interlayer spacing and morphological changes (such as contact at the grain boundaries) that interfere with inter-sheet interactions have the most significant impact on the conductivity of the material.
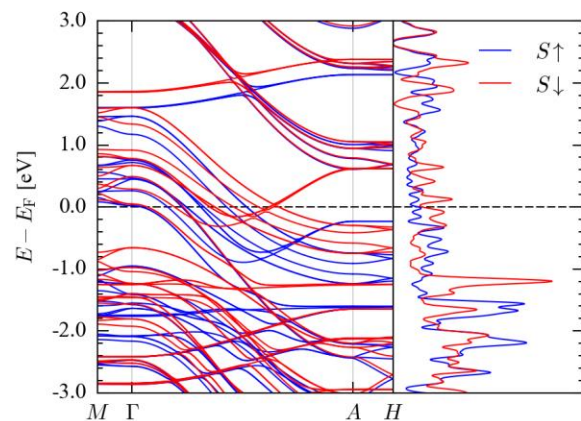

Figure 4. Calculated electronic dispersion and density-of-states curve for **1**.

In order to rationalize these observations in terms of the electronic structure of the framework, DFT calculations were performed (see SI). The calculated band dispersion and density of states (DOS; Figure 4) indicates the compound is actually a semi-metal, with a small DOS at the Fermi energy (E_F) in both spin channels. There is a large dispersion of ~2 eV along the Γ-A line in the Brillouin zone, corresponding to the c-axis in real space. The smallest calculated carrier effective mass for the metallic bands of 0.29 m$_e$ (see SI) suggest facile transport along this direction, and contrasts with a minimum effective mass of 1.27 m$_e$ along the in-plane directions. The bands making up the metallic states correspond to π-type crystal orbitals centered on the metal ions and ligand S atoms, which explains the large dispersion and suggests that the primary mechanism for conductivity is through conductive pathways along the c-axis. This is despite fairly strong covalent bonding between the metal and ligand, as inferred from a Bader-charge analysis (see SI).[16]
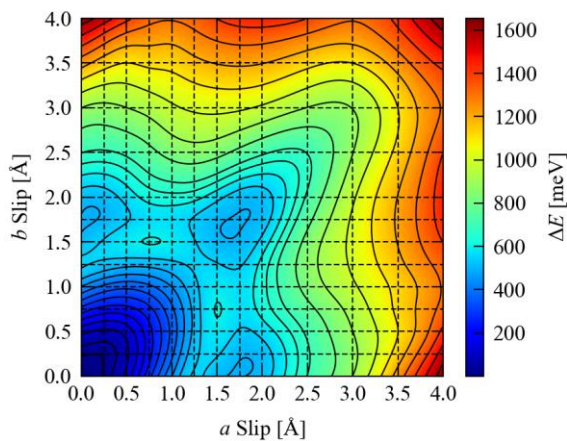
Figure 5. Contour map of the potential energy surface for offsets of alternate layers along the *a* and *b* axes in **1**.

To further investigate the stacking mode in **1**, potential energy surface (PES) calculations were performed on a bi-layer model with offsets of up to 4 Å along the *a* and *b* axes (Figure 5). These studies show that the fully-eclipsed AA structure is the most energetically favored, although a relatively shallow local minimum is present at offsets of ~1.75 Å along one or both axes. Displacements of ±0.25 Å along either or both axes would easily be possible given the thermal energy available at 300 K. These findings also offer some mechanistic insight into the temperature-induced semiconductor-to-metal transition. Thermal expansion along the *c*-direction, or stacking faults leading to misalignment of the layers, were found to introduce a gap in the conduction states (Figures S27–30), which, in combination with a change in the Fermi level, or other factors such as the behavior of the guest molecules in the pore, could play a role in the transition to a narrow-gap semiconductor.

Metallic conductivity has been suggested previously in a nickel benzenehexathiolate framework using first-principles band structure calculations; however, conductivity measurements on a single microflake revealed semiconducting behavior with a small activation energy (E_a) of 26 meV.[7c] The discrepancy was attributed to structural disorder in the sample.[7c] Moreover, DFT calculations performed on $Ni_3(HITP)_2$ framework suggested that the bulk form is metallic, whereas the monolayer form showed a small band gap of 0.25 eV.[7e] The most energetically favored structure for $Ni_3(HITP)_2$ was reported to be an AB slipped-parallel stacking mode wherein one layer was slipped relative to the neighboring one by 1.8 Å along the *a* or *b* vectors.[7a] Additionally, metal substitution was shown by DFT studies to promote or change the electronic properties of these 2D frameworks from semiconducting to metallic.[7e,16-17]

CONCLUSIONS

In summary, we have investigated the temperature-dependent resistivity of a cobalt 2,3,6,7,10,11-triphenylenehexathiolate framework. Variable temperature resistivity studies performed on a pressed-powder pellet indicate a semiconducting phase between 300 K and 170 K, followed by a transition to metallic behavior at temperatures below 130 K, which has been unprecedented in MOFs. A similar transition is observed for films, with the transition temperature being highly dependent on the film thickness.

Electronic-structure calculations support the experimentally observed complex metallic conductivity, with the highest mobility pathways occurring between the sheets. The temperature-dependence of the resistivity exhibits multiple maxima, which suggests that contributions from stacking faults, local molecular vibrations, and the behavior of solvent molecules in the pores may all be convoluted together to produce a complex mechanism for scattering the charge carriers.

Overall, these results identify the first experimentally observed MOF that exhibits band-like metallic conductivity, and highlights the importance of external factors like guest molecules and film morphology in obtaining highly conductive 2D frameworks. We expect the design principles discovered in these fundamental studies to have a profound impact in understanding the charge transport characteristics of MOFs, leading to new materials with impressive electrical properties.

ASSOCIATED CONTENT

Supporting Information. Additional procedures and data, and spectroscopic characterization. This material is available free of charge via the Internet at http://pubs.acs.org. Data from the computational modelling is available online free of charge at [URL to be added on acceptance].

AUTHOR INFORMATION

Corresponding Authors

* smarines@usc.edu; melot@usc.edu.

ACKNOWLEDGMENTS

REFERENCES

(1) (a) Gray, H. B. *Nat. Chem.* **2009**, *1*, 7; (b) Roger, I.; Shipman, M. A.; Symes, M. D. *Nat. Rev. Chem.* **2017**, *1*, 0003; (c) Seh, Z. W.; Kibsgaard, J.; Dickens, C. F.; Chorkendorff, I.; Nørskov, J. K.; Jaramillo, T. F. *Science* **2017**, *355*.
(2) McKone, J. R.; Marinescu, S. C.; Brunschwig, B. S.; Winkler, J. R.; Gray, H. B. *Chem. Sci.* **2014**, *5*, 865.
(3) O'Keeffe, M.; Yaghi, O. M. *Chem. Rev.* **2012**, *112*, 675.
(4) (a) Hendon, C. H.; Tiana, D.; Walsh, A. *Phys. Chem. Chem. Phys.* **2012**, *14*, 13120; (b) Talin, A. A.; Centrone, A.; Ford, A. C.; Foster, M. E.; Stavila, V.; Haney, P.; Kinney, R. A.; Szalai, V.; Gabaly, F. E.; Yoon, H. P.; Léonard, F.; Allendorf, M. D.

Science **2014**, *343*, 66; (c) Leong, C. F.; Usov, P. M.; D'Alessandro, D. M. *MRS Bulletin* **2016**, *41*, 858; (d) Dolgopolova, E. A.; Brandt, A. J.; Ejegbavwo, O. A.; Duke, A. S.; Maddumapatabandi, T. D.; Galhenage, R. P.; Larson, B. W.; Reid, O. G.; Ammal, S. C.; Heyden, A.; Chandrashekhar, M.; Stavila, V.; Chen, D. A.; Shustova, N. B. *J. Am. Chem. Soc.* **2017**, *139*, 5201; (e) Stassen, I.; Burtch, N.; Talin, A.; Falcaro, P.; Allendorf, M.; Ameloot, R. *Chem. Soc. Rev.* **2017**, *46*, 3185.

(5) (a) Cote, A. P.; Benin, A. I.; Ockwig, N. W.; O'Keeffe, M.; Matzger, A. J.; Yaghi, O. M. *Science* **2005**, *310*, 1166; (b) Makiura, R.; Motoyama, S.; Umemura, Y.; Yamanaka, H.; Sakata, O.; Kitagawa, H. *Nat. Mater.* **2010**, *9*, 565; (c) Colson, J. W.; Woll, A. R.; Mukherjee, A.; Levendorf, M. P.; Spitler, E. L.; Shields, V. B.; Spencer, M. G.; Park, J.; Dichtel, W. R. *Science* **2011**, *332*, 228; (d) Kambe, T.; Sakamoto, R.; Hoshiko, K.; Takada, K.; Miyachi, M.; Ryu, J. H.; Sasaki, S.; Kim, J.; Nakazato, K.; Takata, M.; Nishihara, H. *J. Am. Chem. Soc.* **2013**, *135*, 2462; (e) So, M. C.; Jin, S.; Son, H.-J.; Wiederrecht, G. P.; Farha, O. K.; Hupp, J. T. *J. Am. Chem. Soc.* **2013**, *135*, 15698.

(6) (a) Kobayashi, Y.; Jacobs, B.; Allendorf, M. D.; Long, J. R. *Chem. Mater.* **2010**, *22*, 4120; (b) Wan, S.; G andara, F.; Asano, A.; Furukawa, H.; Saeki, A.; Dey, S. K.; Liao, L.; Ambrogio, M. W.; Botros, Y. Y.; Duan, X.; Seki, S.; Stoddart, J. F.; Yaghi, O. M. *Chem. Mater.* **2011**, *23*, 4094; (c) Hmadeh, M.; Lu, Z.; Liu, Z.; Gandara, F.; Furukawa, H.; Wan, S.; Augustyn, V.; Chang, R.; Liao, L.; Zhou, F.; Perre, E.; Ozolins, V.; Suenaga, K.; Duan, X.; Dunn, B.; Yamamto, Y.; Terasaki, O.; Yaghi, O. M. *Chem. Mater.* **2012**, *24*, 3511; (d) Cai, S.-L.; Zhang, Y.-B.; Pun, A. B.; He, H.; Yang, J.; Toma, F. M.; Sharp, I. D.; Yaghi, O. M.; Fan, J.; Zheng, S.-R.; Zhang, W.-G.; Liu, Y. *Chem. Sci.* **2014**, *5*, 4693; (e) Sun, L.; Campbell, M. G.; Dincă, M. *Angew. Chem. Int. Ed.* **2016**, *55*, 2; (f) Cui, J.; Xu, Z. *Chem. Commun.* **2014**, *50*, 3986; (g) Darago, L. E.; Aubrey, M. L.; Yu, C. J.; Gonzalez, M. I.; Long, J. R. *J. Am. Chem. Soc.* **2015**, *137*, 15703.

(7) (a) Sheberla, D.; Sun, L.; Blood-Forsythe, M. A.; Er, S.; Wade, C. R.; Brozek, C. K.; Aspuru-Guzik, A.; Dincă, M. *J. Am. Chem. Soc.* **2014**, *136*, 8859; (b) Campbell, M. G.; Sheberla, D.; Liu, S.; Swager, T. M.; Dincă, M. *Angew. Chem. Int. Ed.* **2015**, *54*, 4349; (c) Kambe, T.; Sakamoto, R.; Kusamoto, T.; Pal, T.; Fukui, N.; Hoshiko, K.; Shimojima, T.; Wang, Z.; Hirahara, T.; Ishizaka, K.; Hasegawa, S.; Liu, F.; Nishihara, H. *J. Am. Chem. Soc.* **2014**, *136*, 14357; (d) Huang, X.; Sheng, P.; Tu, Z.; Zhang, F.; Wang, J.; Geng, H.; Zou, Y.; Di, C.; Yi, Y.; Sun, Y.; Xu, W.; Zhu, D. *Nat. Commun.* **2015**, *6*, 1; (e) Foster, M. E.; Sohlberg, K.; Spataru, C. D.; Allendorf, M. D. *J. Phys. Chem. C* **2016**, *120*, 15001.

(8) Clough, A. J.; Yoo, J. W.; Mecklenburg, M. H.; Marinescu, S. C. *J. Am. Chem. Soc.* **2015**, *137*, 118.

(9) (a) Lin, S.; Diercks, C. S.; Zhang, T.-B.; Kornienko, N.; Nichols, E. M.; Zhao, Y.; Paris, A. R.; Kim, D.; Yang, P.; Yaghi, O. M.; Chang, C. J. *Science* **2015**, *349*, 1208; (b) Hod, I.; Sampson, M. D.; Deria, P.; Kubiak, C. P.; Farha, O. K.; Hupp, J. T. *ACS Catal.* **2015**, *5*, 6302; (c) Miner, E. M.; Fukushima, T.; Sheberla, D.; Sun, L.; Surendranath, Y.; Dincă, M. *Nat. Commun.* **2016**, *7*, 10942; (d) Dong, R.; Pfeffermann, M.; Liang, H.; Zheng, Z.; Zhu, X.; Zhang, J.; Feng, X. *Angew. Chem. Int. Ed.* **2015**, *54*, 12058; (e) Dong, R.; Zheng, Z.; Tranca, D. C.; Zhang, J.; Chandrasekhar, N.; Liu, S.; Zhuang, X.; Seifert, G.; Feng, X. *Chem. Eur. J.* **2017**, *23*, 2255.

(10) (a) Cairns, A. B.; Goodwin, A. L. *Chem. Soc. Rev.* **2013**, *42*, 4881; (b) Ramesh, T. N.; Jayashree, R. S.; Kamath, P. V. *Clays Clay Miner.* **2003**, *51*, 570.

(11) Orchard, A. F. *Magnetochemistry*; Oxford University Press, 2003.

(12) (a) Ray, K.; Begum, A.; Weyhermüller, T.; Piligkos, S.; Slageren, J. v.; Neese, F.; Wieghardt, K. *J. Am. Chem. Soc.* **2005**, *127*, 4403; (b) Sproules, S.; Wieghardt, K. *Coord. Chem. Rev.* **2011**, *255*, 837.

(13) Smith, C. E.; Odoh, S. O.; Ghosh, S.; Gagliardi, L.; Cramer, C. J.; Frisbie, C. D. *J. Am. Chem. Soc.* **2015**, *137*, 15732.

(14) (a) Corr, S. A.; Shoemaker, D. P.; Melot, B. C.; Seshadri, R. *Phys. Rev. Lett.* **2010**, *105*, 056404; (b) Goodenough, J. B. *J. Solid State Chem.* **1971**, *3*, 490; (c) Park, J.; Oh, I. H.; Lee, E.; Lee, K. W.; Lee, C. E.; Song, K.; Kim, Y.-J. *Appl. Phys. Lett.* **2007**, *91*, 153112.

(15) (a) Hartmann, B.; Müller, J.; Sasaki, T. *Phys. Rev. B* **2014**, *90*, 195150; (b) Kato, R. *Chem. Rev.* **2004**, *104*, 5319.

(16) Shojaei, F.; Hahn, J. R.; Kang, H. S. *Chem. Mater.* **2014**, *26*, 2967.

(17) (a) Chen, S.; J., D.; Zeng, X. C. *Phys. Chem. Chem. Phys.* **2015**, *17*, 5954; (b) Chakravarty, C.; Mandal, B.; Sarkar, P. *J. Phys. Chem. C* **2016**, *120*, 28307; (c) Sun, L.; Hendon, C. H.; Park, S. S.; Tulchinsky, Y.; Wan, R.; Wang, F.; Walsh, A.; Dincă, M. *Chem. Sci.* **2017**, *8*, 4450.

Table of contents graphic:
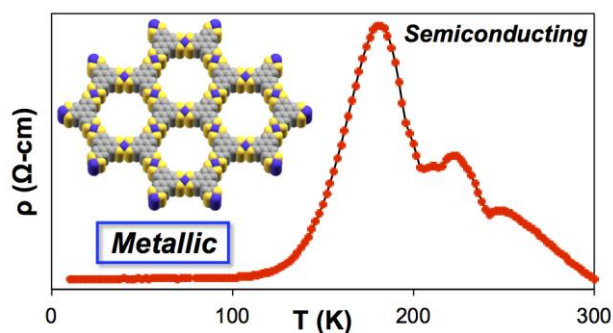
Metallic Conductivity in a Two-Dimensional Cobalt Dithiolene Metal-Organic Framework

Andrew J. Clough,‡ Jonathan M. Skelton,† Courtney A. Downes,‡ Ashley de la Rosa,‡ Joseph W. Yoo,‡ Aron Walsh,† Brent C. Melot,‡* and Smaranda C. Marinescu‡*

‡Department of Chemistry, University of Southern California, Los Angeles, California 90089, United States

†Department of Materials, Imperial College London, London, UK

* E-mail: smarines@usc.edu; melot@usc.edu.

General

All manipulations of air and moisture sensitive materials were conducted under a nitrogen atmosphere in a Vacuum Atmospheres drybox or on a dual manifold Schlenk line. The glassware was oven-dried prior to use. Acetonitrile and dichloromethane were degassed with nitrogen and passed through activated alumina columns and stored over 4 Å Linde-type molecular sieves. Ethyl acetate, water, and ethanol were placed under vacuum and refilled with nitrogen (10 ×). Deuterated solvents were dried over 4 Å Linde-type molecular sieves prior to use. Elemental analyses were performed by Robertson Microlit Laboratories, 1705 U.S. Highway 46, Suite 1D, Ledgewood, New Jersey, 07852. All the chemical regents were purchased from commercial vendors and used without further purification. The ligand 2,3,6,7,10,11-triphenylene-hexathiol[1] (THT) was prepared according to the reported procedures. Water was deionized with the Millipore Milli-Q Synergy system (18.2 MΩ·cm resistivity). All other chemical regents were purchased from commercial vendors and used without further purification.

Synthesis of 1

The cobalt dithiolene framework **1** was prepared according to the reported procedures.[2] A 400 mL glass jar was charged with an aqueous solution of $CoCl_2 \cdot 6H_2O$ (60 mg, 0.25 mmol, 2.5 mM, 100 mL volume). Separately, a suspension of 2,3,6,7,10,11-triphenylene-hexathiol (THT) (10 mg, 0.024 mmol) in N-Methyl-2-pyrrolidone (NMP) (0.2 mL) was then diluted with ethyl acetate until the total volume of the suspension reached 20 mL, sealed, and briefly sonicated to form an uniform suspension. Ethyl acetate (80 mL) was gently added to the aqueous solution to create a liquid-liquid interface; the suspension of THT was then gently added to the ethyl acetate layer and the jar was sealed and allowed to stand overnight. A black film appeared at the liquid-liquid interface over 5 days. The film was deposited on glass supports by pulling the substrate up through the film. The deposited films were then washed with water and allowed to evaporate to dryness. Alternatively, the black solid **1** was collected by filtration and washed with water and methanol for bulk powder analyses.

X-Ray Photoelectron Spectroscopy (XPS)

XPS data were collected using a Kratos AXIS Ultra instrument. The monochromatic X-ray source was the Al K α line at 1486.7 eV, and the hybrid lens and slot mode were used. Low-

resolution survey spectra were acquired between binding energies of 1–1200 eV. Higher-resolution detailed scans, with a resolution of 0.1 eV, were collected on individual XPS regions of interest. The sample chamber was maintained at $< 9 \times 10^{-9}$ Torr. The XPS data were analyzed using the CasaXPS software.

Powder X-ray diffraction (PXRD)
PXRD studies were performed on a Rigaku Ultima IV X-Ray diffractometer in reflectance parallel beam/parallel slit alignment geometry. The measurement employed Cu Kα line focused radiation at 1760 W (40 kV, 44 mA) power and a Ge crystal detector fitted with a 2 mm radiation entrance slit. Samples were mounted on zero-background sample holders and were observed using a 0.08° 2θ step scan from 2.0 – 40.0° with an exposure time of 0.4 s per step. No peaks could be resolved from the baseline for 2θ > 35°.

High resolution synchrotron powder X-ray diffraction data was collected using the 11-BM beamline mail-in program at the Advanced Photon Source (APS), Argonne National Laboratory, with an average wavelength of 0.414575 Å. Discrete detectors covering an angular range from 0.5 to 30º 2θ are scanned over a 34º 2θ range, with data points collected every 0.001º 2θ and scan speed of 0.01º/s. An Oxford Cryosystems Cryostream Plus device allowed for sample temperatures to be controlled over a range of 100-295 K.

Modeling
Molecular modeling of the framework **1** was carried out using the Materials Studio (version 8.0) suite of programs by Accelrys. The molecular fragment used to generate the model is shown in Figure S1. The unit cell was constructed starting with a primitive hexagonal unit cell with space group P6/*mmm* using cell parameters $a = b = 22.52$ Å and $c = 3.3$ Å. The structure was optimized with Materials Studio Forcite calculations using geometry optimization and universal forcefield methods. The MS Reflex module was used to calculate the expected PXRD patterns. Line broadening for crystallite size was not calculated. Comparison of the simulated and experimental PXRD patterns verified the simulated structure.

Conductivity Measurements
Conductivity measurements were performed using a custom set up integrated into a 14T Quantum Design Dynacool Physical Properties Measurement System. A Keithley 6220 Precision Current Source (excitation currents of 1-50 nA) was used to trigger and control a Keithley 2182A nanovoltmeter. In order to minimize errors associated with contact resistance and drift voltages, a Keithley 2172 matrix switch equipped with a Keithley 6536 Hall effect card was used to alternate the direction of the applied current. Because of difficulty associated with preparing samples with uniform dimensions, all measurements were performed in a four-point probe Van der Pauw geometry. Copper wire contacts were attached to the films using a conductive carbon paint and soldered onto a Quantum Design puck with resistivity option. All measurements were performed under a reduced pressure of ~10 torr.

Scanning Electron Microscopy (SEM)
SEM images were collected using a JEOL-7001F operating at 15 kV with 5 nA of probe current.

Atomic Force Microscopy (AFM)
AFM topography images were collected in tapping mode using an Agilent 5420 SPM instrument

operating in tapping mode. The probe tips were Tap300-G Silicon AFM probes (resonant frequency 300 kHz, force constant 40 N/m) purchased from Budgetsensors.com and aligned prior to use. Images were collected with a scan rate of 0.1 lines per second and over an area of 40 µm. All samples were imaged under one atmosphere of air at room temperature.

Gas sorption analysis
Brunauer-Emmett-Teller (BET) measurements were performed on a Nova 2200e surface area and pore size analyzer (Quantachrome Instruments, Inc.). Samples were degassed for 2 h at 150 °C in vacuo prior to measurements.

Computational Modeling
Density-functional theory calculations on the crystal structure of Framework **1** were carried out within the plane-wave pseudopotential formalism, as implemented in the Vienna *ab initio* Simulation Package (VASP) code.[3]

We employed the PBEsol exchange-correlation functional[4] with the DFT-D3 dispersion correction.[5] The ions were modelled with projector augmented-wave (PAW) pseudopotentials[6] treating the H 1s, C 2s and 2p, S 3s and 3p and Co 4s, 3d and 3p electrons as valence states. A kinetic-energy cutoff of 800 eV was used to define the plane-wave basis, and the electronic Brillouin zone was integrated using Γ-centered Monkhorst-Pack k-point meshes[7] with 1×1×5 and 2×2×15 subdivisions for geometry optimisations and electronic-structure calculations, respectively. Careful convergence testing found that the 1×1×5 mesh was sufficient to converge the absolute value of the total energy and unit-cell pressure to within 1 meV per atom and 1 kbar (0.1 GPa), respectively, while the denser mesh was required to obtain a high-quality electronic density of states and an accurate Fermi energy.

Tolerances of 10^{-8} eV and 10^{-2} eV Å^{-1} were applied during the optimisation of the Kohn-Sham wavefunctions and atom positions and cell parameters, respectively. The PAW projection was performed in real space. The precision of the charge-density grids was set automatically to avoid aliasing errors. For the electronic-structure calculations, a Gaussian smearing with a width, σ, of 0.05 eV was used to broaden the density of states (DoS), and band dispersions were obtained by calculating eigenvalues non-self consistently at strings of k-points along the high-symmetry paths through the Brillouin zone.
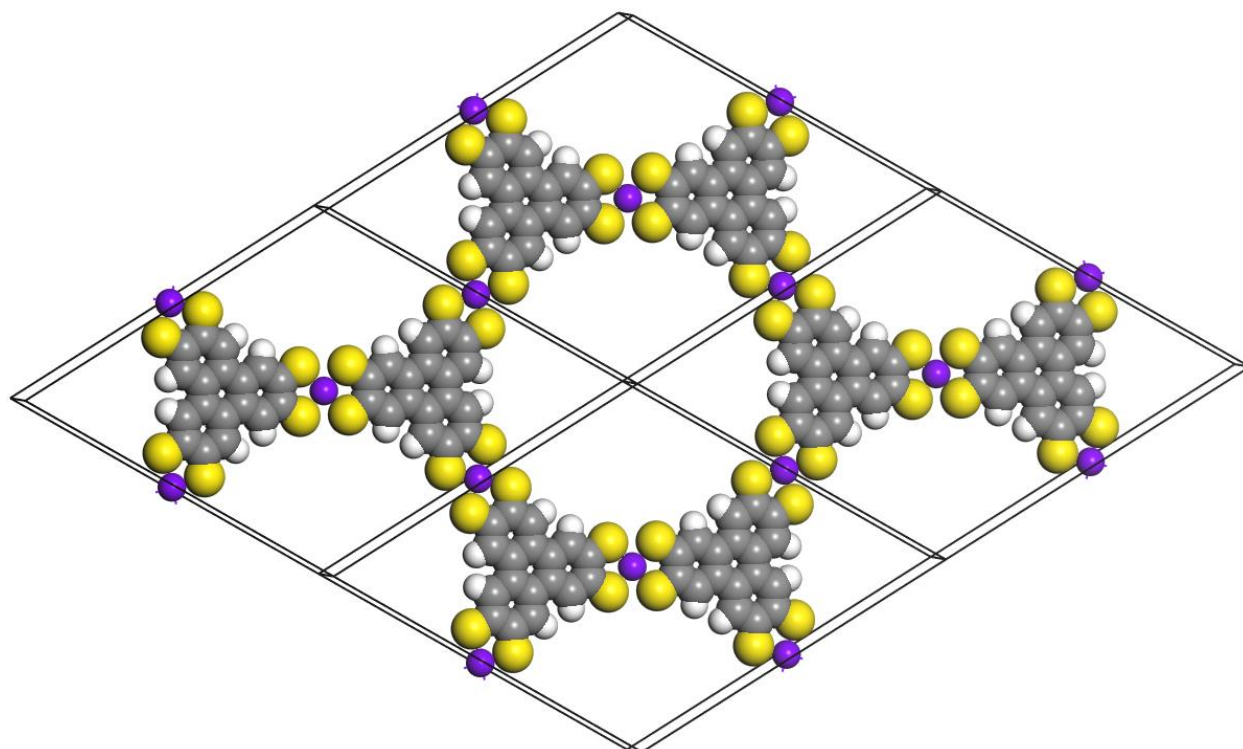
Figure S1. Spacefilling illustration of the fragment used to generate the model unit cell.
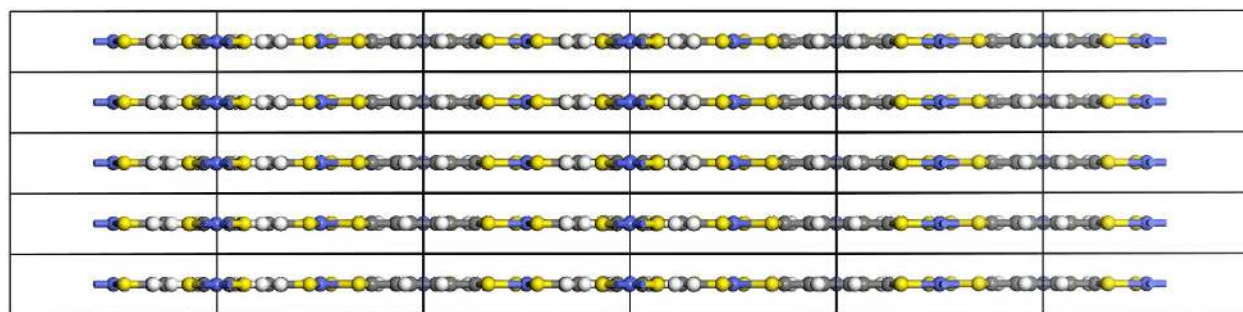

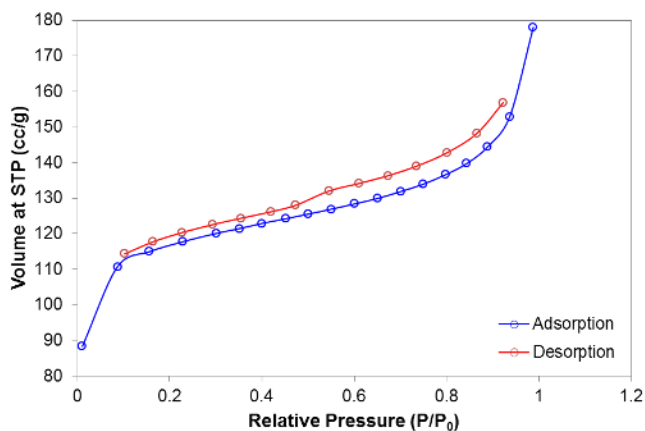**Figure S2.** Model structures of the eclipsed pattern.

Figure S3. Nitrogen sorption isotherms performed on **1** at 77 K reveal a Brunauer-Emmett-Teller surface area of 370(5) m^2 g^{-1}.
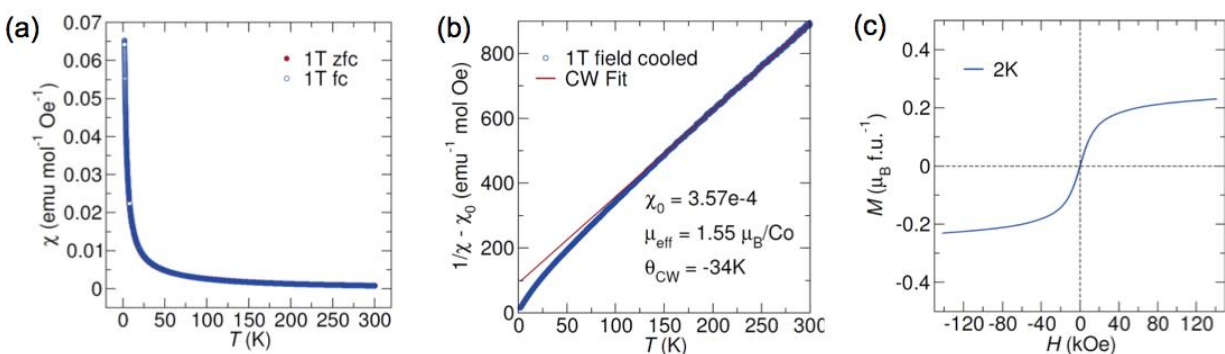

Figure S4. Magnetic studies performed on the cobalt dithiolene framework **1**. (a) Magnetic susceptibility data for **1**; (b) Curie-Weiss fit to the data; and (c) Magnetization (*M*) versus applied magnetic field (*H*) data for **1**.
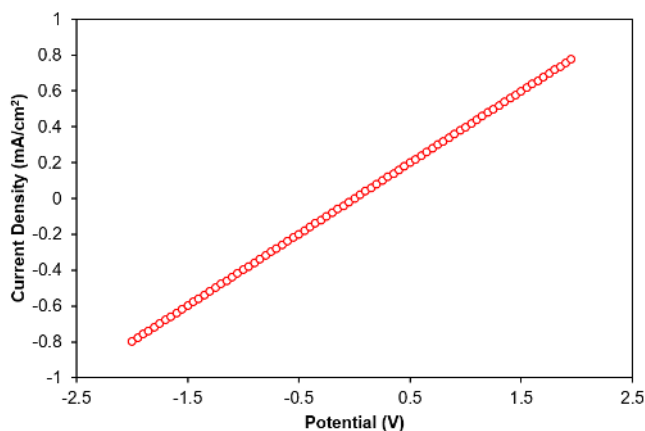
Figure S5. Room temperature I-V trace of solid **1** pressed in a pellet of 0.24(2) mm thickness, which displays Ohmic response between –2.0 and +2.0 V.
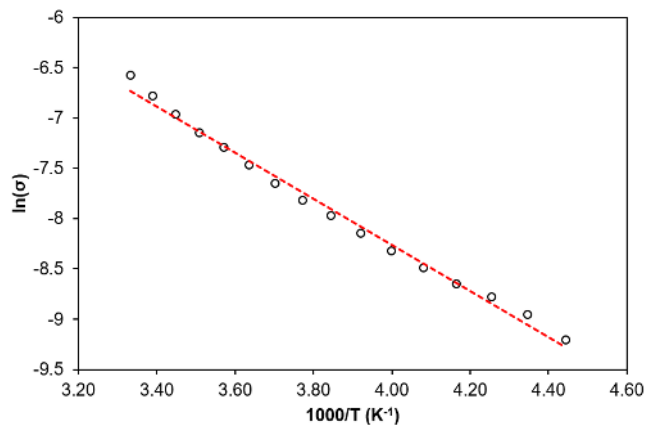
Figure S6. Arrhenius plot of the high temperature conductivity data of solid **1** pressed in a pellet of 0.24(2) mm thickness, displaying an activation energy (E_a) of 173 meV.
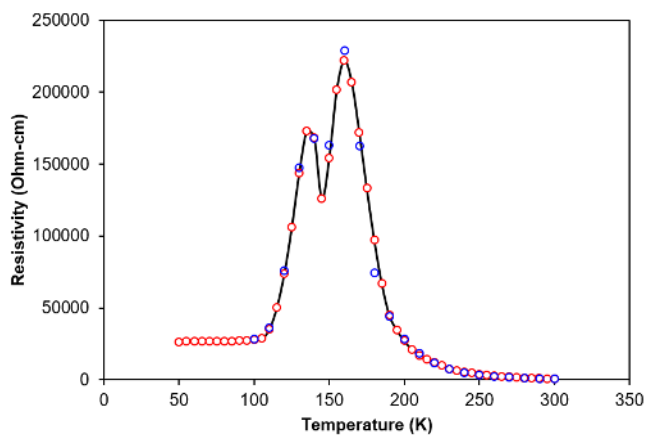

Figure S7. Overlay of the variable-temperature resistivity data for solid **1** pressed in a pellet of 0.24(2) mm upon cooling (blue) and warming (red). The resistivity data of the pressed-pellet was measured at temperatures ranging from 300 to 60 K. Below 60 K the carbon paint stopped maintaining physical contact with the sample.
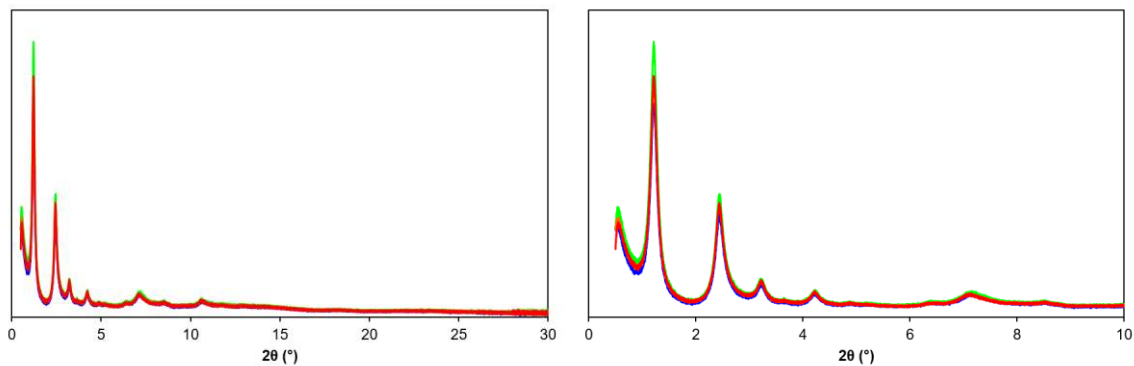
Figure S8. Synchrotron variable temperature powder X-ray diffraction (PXRD) patterns of solid **1** collected at 100 (blue), 200 (green), 280 (orange), and 295 (red) K. No peaks could be resolved from the baseline for $2\theta > 12°$.
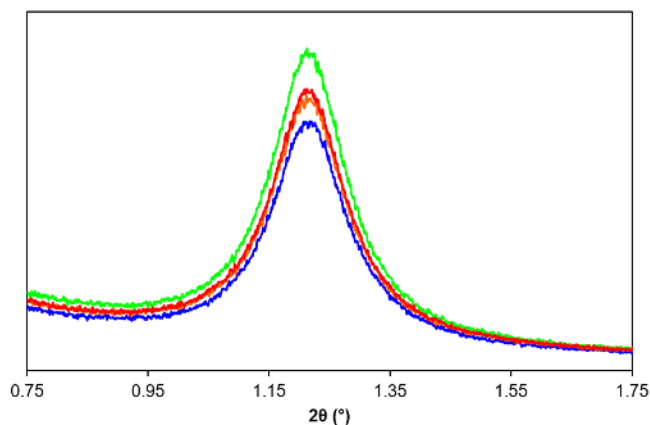

Figure S9. Overlay of the variable temperature PXRD patterns of **1** focusing on the [100] reflections collected at 100 (blue), 200 (green), 280 (orange), and 295 (red) K.
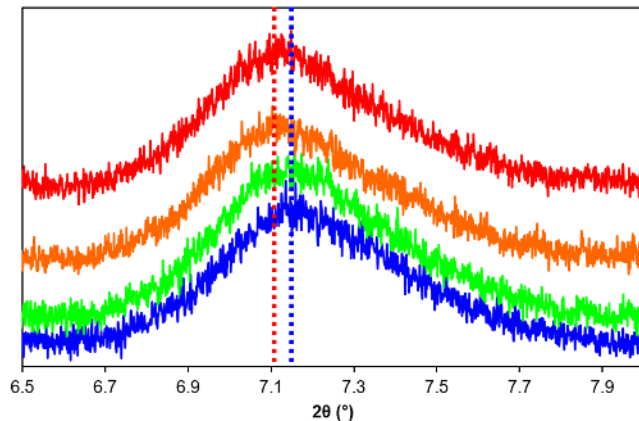

Figure S10. Overlay of the variable temperature PXRD patterns of **1** focusing on the [001] reflections collected at 100 (blue), 200 (green), 280 (orange), and 295 (red) K.
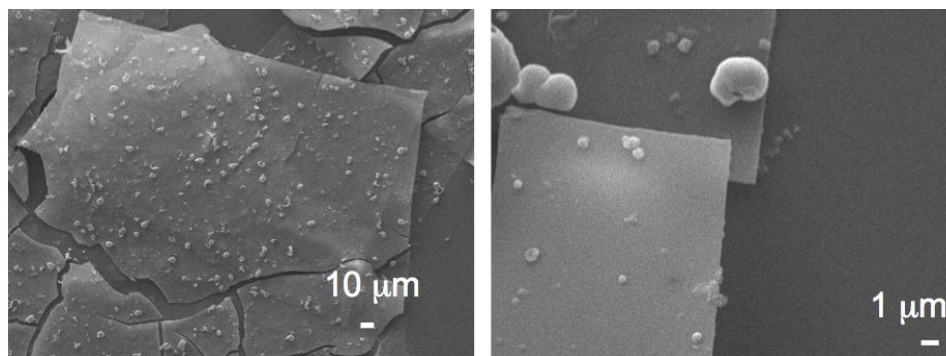
Figure S11. Scanning Electron Microscope (SEM) images of the cobalt dithiolene film **1** on glass support (15 kV accelerating voltage).
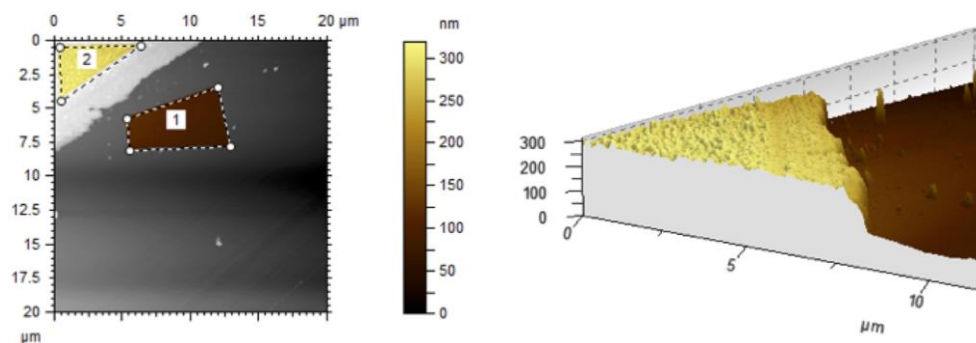

Figure S12. Atomic Force Microscopy (AFM) studies of the cobalt dithiolene film **1** of 0.20(2) μm thickness on glass.
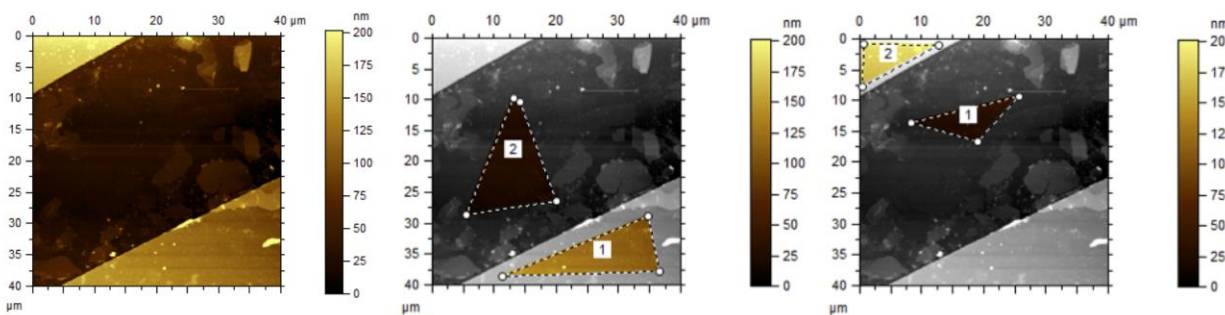

Figure S13. Atomic Force Microscopy (AFM) studies of the cobalt dithiolene film **1** of 0.12(1) μm thickness on glass.
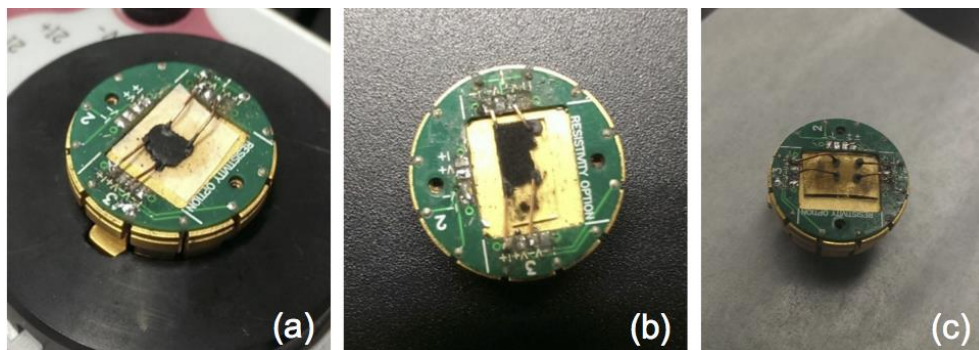
Figure S14. Images of the samples – pellet (a) or films of **1** (b) and (c) – and their puck assemblies for conductivity measurements. Graphitic carbon paint was used to create Ohmic contacts.
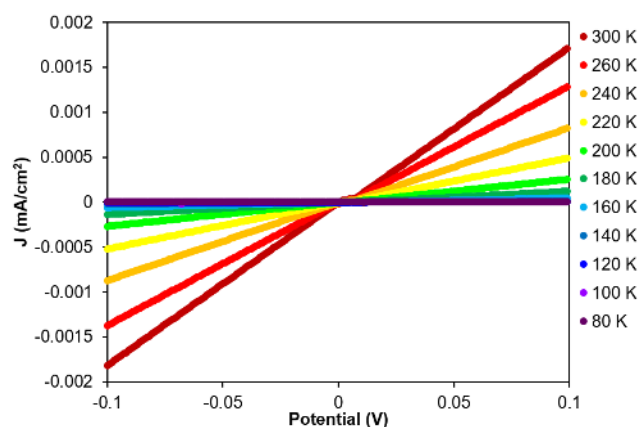

Figure S15. Typical variable temperature I-V traces of the cobalt dithiolene film **1** on a glass support, displaying Ohmic response between –0.1 and +0.1 V.
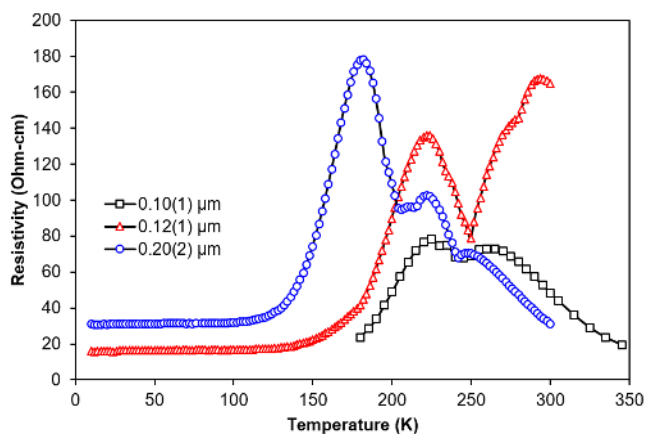

Figure S16. Variable-temperature resistivity data for films **1** with thicknesses of 0.10(1) (black), 0.12(1) (red), and 0.20(2) (blue) μm deposited on glass supports. The resistivity data of the film with a 0.10(1) μm thickness was measured at temperatures ranging from 350 to 180 K. Below 180 K the carbon paint stopped maintaining physical contact with the sample.
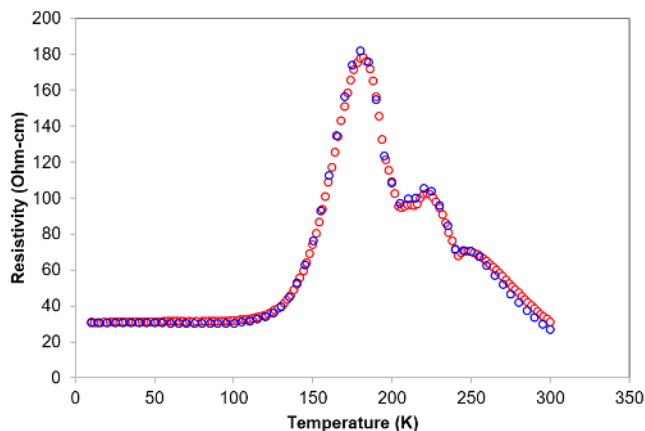
Figure S17. Overlay of the variable-temperature resistivity data for the cobalt dithiolene film of **1** with a thickness of 0.20(2) μm deposited on glass supports, upon cooling (blue) and warming (red).
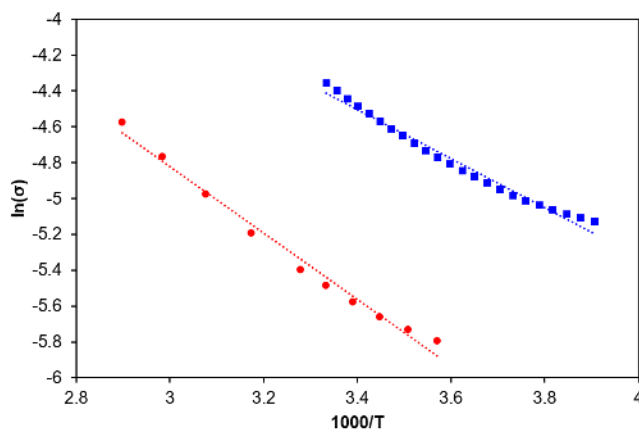

Figure S18. Arrhenius plots of the high temperature conductivity data of the cobalt dithiolene film **1** of 0.10(1) (red) and 0.20(2) (blue) μm thicknesses on glass supports, displaying activation energies (E_a) of 159 and 118 meV, respectively.

Entry	Sample	Thickness	$T_{metallic}$ (K)	Resistivity (kΩ-cm) at 300 K	Conductivity (mS·cm^{-1}) at 300 K	E_a (meV)
1	pellet **1**	0.24(2) mm	135	0.720	1.4	173
2	film **1**	0.10(1) μm	225	0.048	21	159
3	film **1**	0.12(1) μm	222	0.167	6.0	–
4	film **1**	0.20(2) μm	180	0.031	32	118

Table S1. Selected parameters for the variable-temperature resistivity analyses performed on a pressed pellet or films of **1**. $T_{metallic}$ represents the lowest temperature at which the transition between a semiconducting to metallic conductivity occurs.
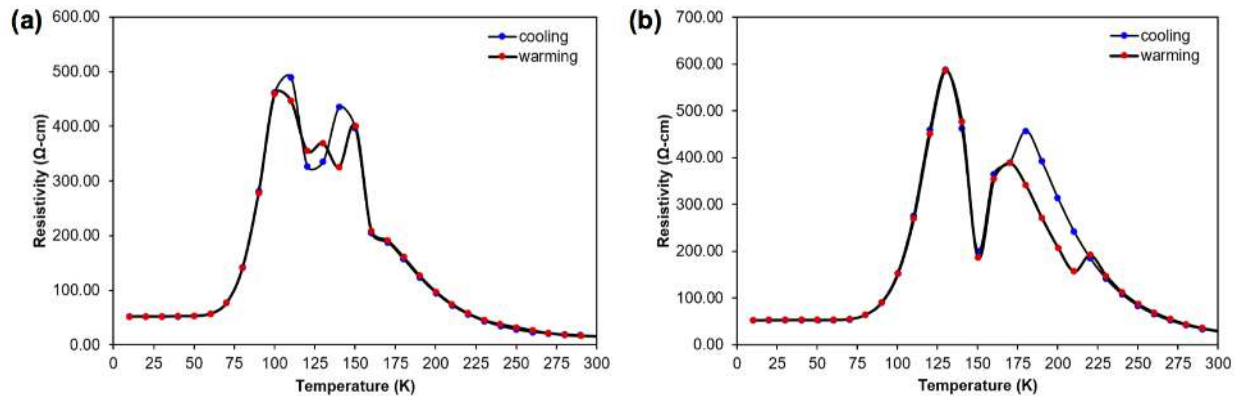
Figure S19. Overlay of the variable-temperature resistivity data for film **1** with a thickness of 0.5(1) µm before (a) and after (b) a two-hour exposure under vacuum at 90 °C, upon cooling (blue) and warming (red).
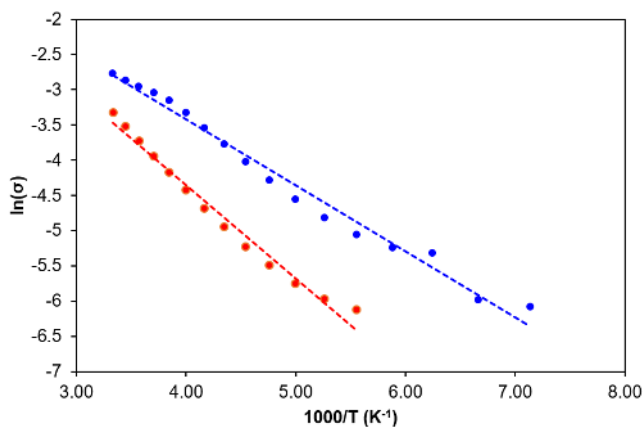

Figure S20. Arrhenius plot of the high temperature conductivity data of film **1** with a thickness of 0.5(1) µm before (blue) and after (red) a two-hour exposure under vacuum at 90 °C, displaying activation energies (E_a) of 81 (before) and 114 (after) meV.
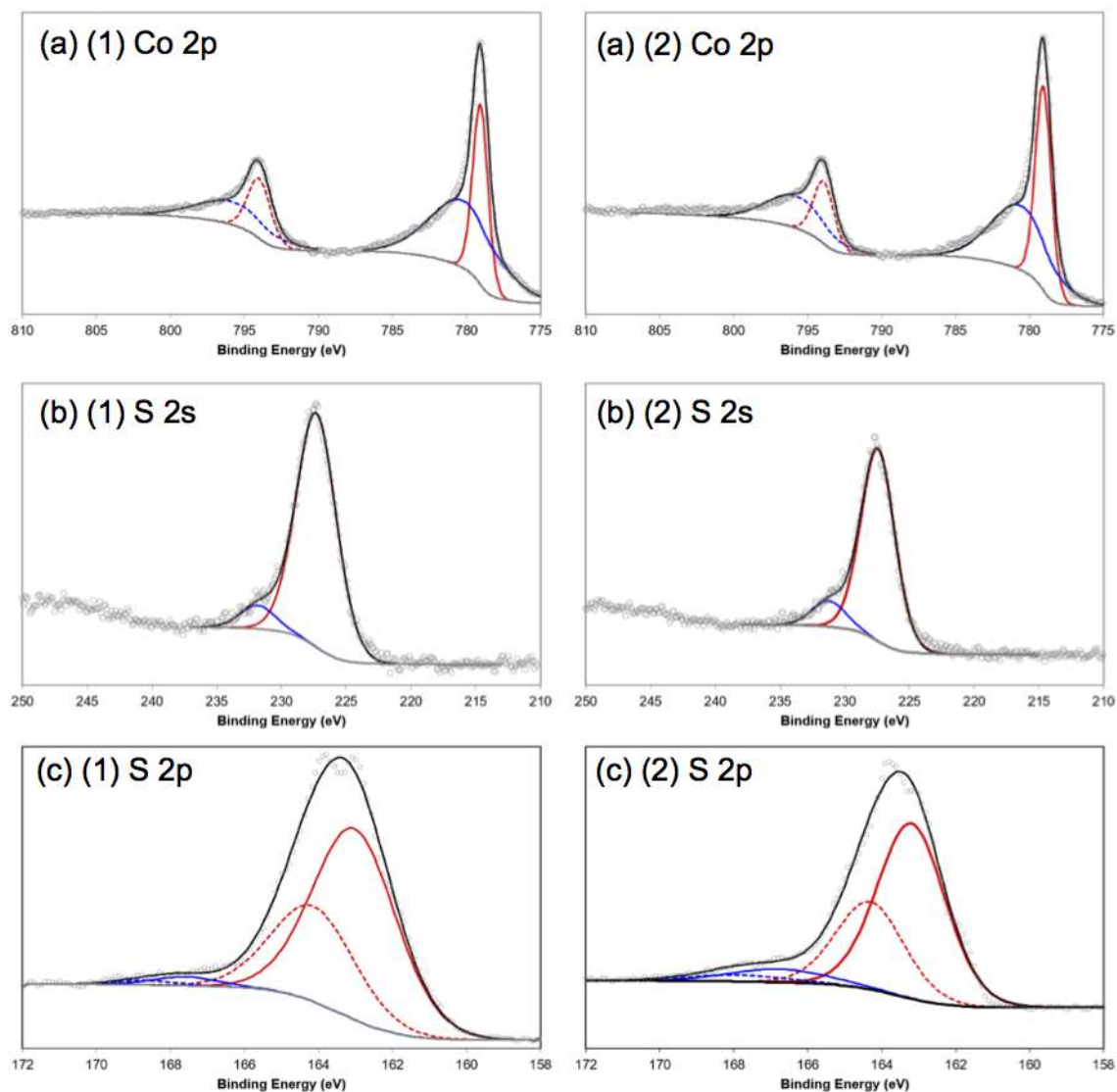
Figure S21. X-ray photoelectron spectroscopy (XPS) data of the cobalt dithiolene film **1** collected at room temperature (1) before and (2) after conductivity measurements. XPS data from top: (a) Co 2p, (b) S 2s, and (c) S 2p.

Magnetic Structure and Equilibrium Geometry

Given the complex magnetic structure of Framework **1**, we performed a series of calculations with different initial magnetic moments and compared the spin density and total energies of the resulting electronic groundstates.

We performed two initial calculations starting with an 0 and 1 unpaired spin(s) on each ion (i.e. on the Co ions *and* the ligand atoms), and allowed the spin density to relax during the wavefunction optimisation. We then performed a series of additional calculations starting from one of seven initial moments corresponding to Co^{2+} and Co^{3+} ions with unpaired spin density distributed among the bonded S atoms as appropriate for a thiolate anion/radical configuration

(Figure S22). In these calculations, the total magnetic moment was either fixed to the initial value or allowed to relax during the minimisation.

We found five unique magnetic configurations, of which the lowest energy had a total moment of 3.8 BM per unit cell with approx. 0.9 BM (one unpaired electron) associated with each Co ion and the remaining density associated with the S and C atoms of the ligands. A larger proportion of the unpaired spin density on the ligand was assigned to S than to C, and each S atom had an equal magnetic moment. This state can thus be assigned as Co^{2+} ions with each of the S atoms on the ligand being of mixed ion/radical character.
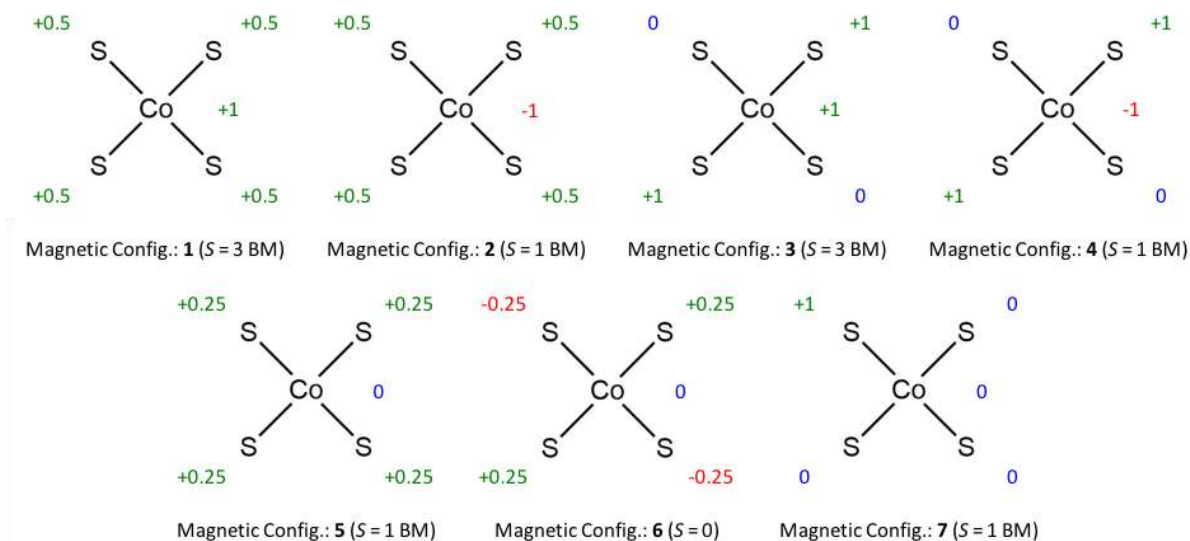

Figure S22. Initial local magnetic moments and nominal total moments of seven magnetic configurations tested during preliminary calculations to determine the optimum magnetic configuration of the unit cell of Framework **1**.

We next performed further calculations in which the seven local magnetic configurations in Figure S22 were arranged in a frustrated antiferromagnetic configuration, with the sign of the initial moments reversed on one of the three Co ions in the unit cell. These yielded a further four unique magnetic configurations, none of which were lower in energy than the ferromagnetic state.

Optimisation of the atomic positions and unit-cell parameters with the most energetically-favourable initial configuration yielded a structure close to the experimental one (a_{opt} = 23.133 Å, c_{opt} = 3.140 Å; c.f. a = 22.52 Å, c = 3.3 Å from the experimental measurements). Moreover, the spin density relaxed during the geometry optimisation to a final value of 1.8 BM, which is in good agreement with the moment of 1.5 BM per formula unit measured experimentally. Analysis of the spin density yielded local moments of ~0.6 BM on each Co ion, with negligible spin density on the ligands (Figure S23).

A single-point calculation on the optimised cell starting with an antiferromagnetic arrangement of the Co spins produced a configuration 72 meV per Co ion higher in energy than the ferromagnetic arrangement, confirming the latter to be the groundstate.

Finally, we also performed calculations on a model with a $-3\ e$ charge per unit cell on the framework and a homogenous compensating background charge, which would allow for three Co^{3+} ions with dianionic dithiolate ligands. This configuration proved to be unstable during geometry optimisation, however, and resulted in layer separation (c_{opt} = 14.963 Å). This could be indicative of charges on the framework being unstable, but may also reflect the homogenous background charge being a poor model for explicit charge-compensating cations in the pores. We therefore opted to perform calculations on the uncharged model with the ferromagnetic spin configuration.
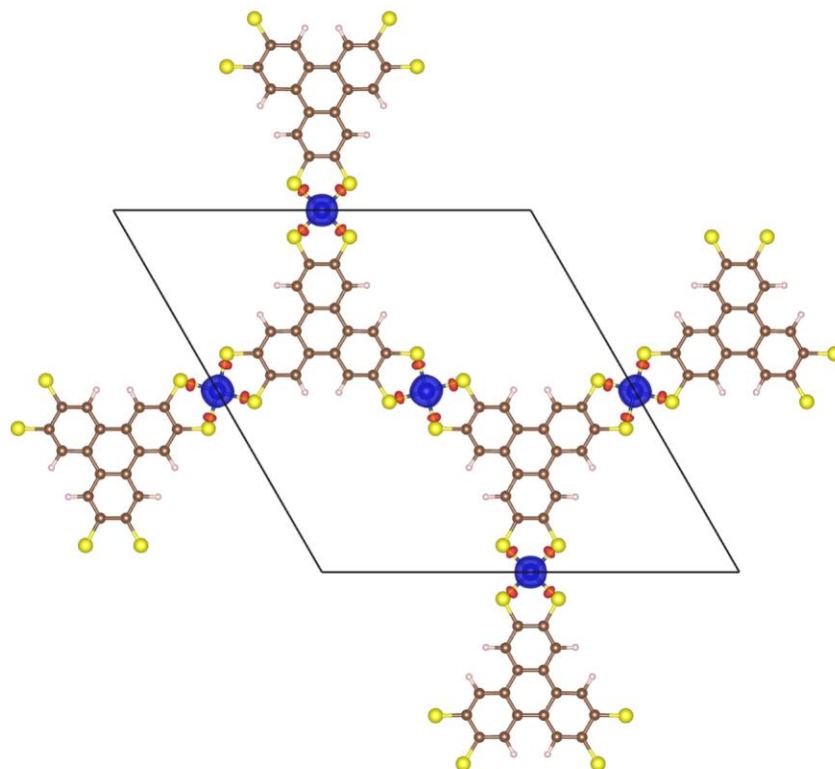
Figure S23. Calculated spin density of the optimised model of Framework **1**. This image was prepared using the VESTA software.[8]

Electronic Structure

As described in the text, electronic-structure calculations on Framework **1** revealed it to be a semi metal, with a small density of states at the Fermi energy and a large dispersion along the real-space c direction.

We estimated the carrier effective masses m^* from the curvature of the band dispersion according to:

$$\frac{1}{m^*} = \frac{1}{\hbar^2} \frac{\partial^2 E(k)}{\partial k^2} \tag{1}$$

where $\hbar$ is the reduced Planck constant. The bands contributing to the metallic states were identified as those crossing the Fermi energy along the Γ-A line in the electronic Brillouin zone within 25 meV of the Fermi energy. The energies of those bands along the M-Γ, Γ-A and A-H segments were then fit to quadratic polynomials of the form $E(k) = ak^2 + bk + c$, from which the second derivative term in Eq. (1) can be extracted as $\partial^2 E(k)/\partial k^2 = 2a$.

Whereas the bands along the M-Γ and A-H segments are well fit by single quadratic functions, the more complex dispersion along the Γ-A segment is highly non-parabolic. We therefore fitted this segment in a "piecewise" fashion to multiple functions, and extracted "local" second derivatives for segments close to the Fermi energy. Some bands along this segment also exhibit sharp band crossings that cannot be fitted to a quadratic function; to avoid including these in the effective-mass calculations, we omitted fits where the maximum absolute error of the fit was greater than 25 meV. The fits used to calculate the effective masses are overlaid on the band structure from Figure 4 in the text in Figure S24.
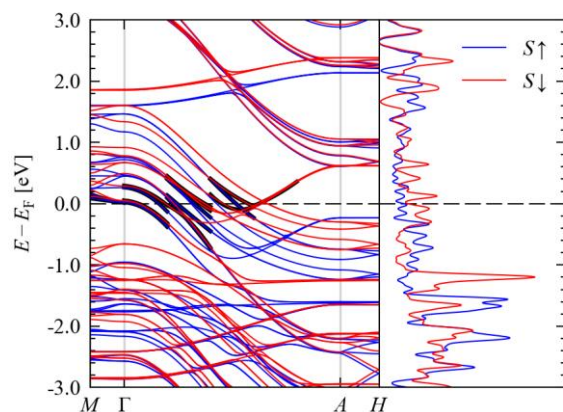
Figure S24. Calculated electronic dispersion and density-of-states curve for Framework **1**. The blue and red lines show the spin-up and spin-down components of the electronic structure, respectively. The thick black overlaid lines illustrate the fitting of the bands contributing to metallic states to quadratic polynomials in order to estimate the carrier effective masses, as described in the text.

From this analysis, the effective masses of the bands near the Fermi energy along the M-Γ segment range from 1.27 to 18.7 m_e in the spin-up channel, while all of the bands in the spin-down channel lie outside of the 25 meV threshold. Along the Γ-A segment, the calculated effective masses range from –0.42 to –1.52 m_e and 1.43 to 8.04 m_e in the spin-up channel, and -0.43 to –0.59 m_e and 0.29 to 7.01 m_e in the spin-down channel. None of the bands along the A-H segment fall within 25 meV of the Fermi energy.

To establish the nature of the conductive states, we identified the partially-occupied bands and calculated an orbital density plot showing the associated crystal orbitals (Figure S25). This analysis shows that the valence orbitals consist mainly of Co d and S p orbitals, with a small contribution from the ligand C p orbitals. This suggests that the primary conduction mechanism is via channels formed of the metal and S valence orbitals.

Although the orbital density plots do not show the phasing of the orbitals, it can be inferred that they are of π symmetry, since the band energies reduce from Γ (in-phase overlap

between unit cells) to *A* (antiphase overlap between unit cells along the *c* direction). The large dispersion of these bands can therefore be explained by a strong interaction between metal centres in alternate layers.

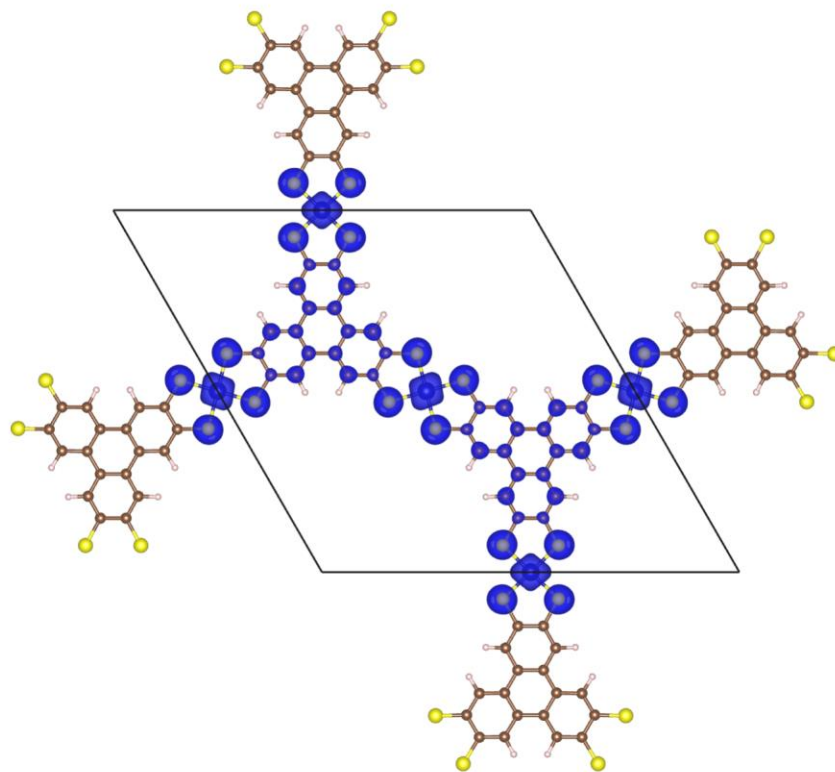**Figure S25.** Orbital-density plot showing the crystal orbitals associated with the partially-occupied bands in the optimised model of Framework **1**. This image was prepared using the VESTA software.[8]

Following literature reports,[9] we also performed a Bader-charge analysis to estimate the charge on the Co ions. We obtained a Bader charge of 0.51 *e* per atom, which, as per the analysis,[9] suggests a predominantly covalent character to the Co-S bonds. Regardless, the band band dispersion clearly indicates that transport along the *c* axis is more facile compared to the in-plane *a* and *b* directions.

Finally, although performing calculations with explicit charge-compensating cations in the pores is infeasible given the lack of crystallographic order, to test the possible effects of reducing the framework on the electronic structure, we recalculated the dispersion and DoS curves in Figure 4 in the text/Figure S24 with a charge of –3 *e* per unit cell and a compensating homogenous background charge (Figure S26).
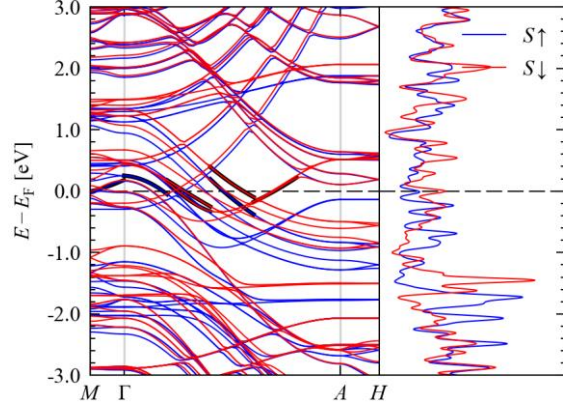
Figure S26. Calculated electronic dispersion and density-of-states curve for Framework **1** with a charge of –3 e per unit cell. As in Figure S24, the blue and red lines show the spin-up and spin-down components of the electronic structure, respectively, and the overlaid black lines illustrate the fitting to estimate the carrier effective masses.

Comparison with Figure 4 in the text suggests that the negative charge leads to additional bands around the Fermi level but, crucially, does not change the metallic nature, nor the large band dispersion along the Γ-A segment. The calculated carrier effective masses are –0.59 and 1.37 m_e in the spin-up channel and 0.75 to 6.71 m_e in the spin-down channel, which are comparable to the values obtained for the neutral cell.

Structural Flexibility

To explore the origin of the metal-to-semiconductor transition in **1**, we performed additional calculations to study the effect of structural deformation on the electronic structure.

To investigate the effect of expansion along the c direction, we performed a series of single-point energy calculations on the optimised model in which the c axis was lengthened by up to 15 Å. To study the effect of layer misalignment, we prepared a 1×1×2 supercell expansion and performed a series of single-point calculations in which one of the two layers was displaced with respect to the other by up to 4 Å along the crystallographic a and b directions. To allow for changes to the equilibrium interlayer spacing, at each a/b displacement we performed a series of calculations with the length of the c axis adjusted by –0.3 to 0.5 Å in 0.1 Å steps. The resulting energy as a function of c-axis length was then interpolated with a cubic spline, and the optimum interlayer spacing and associated total energy obtained by locating the minimum with a binary search.

In the calculations on the single-layer models, we tried both fixing the magnetic moment to the value obtained for the optimised structure (1.8 BM) and allowing it to optimise from an initial configuration with one unpaired spin on each Co ion.

In the single-point calculations on the bilayer model, the k-point mesh was reduced to 1×1×3 subdivisions for the longer c axis. We found in preliminary calculations on a subset of the structures with constrained magnetic moments that misaligning alternate layers had a substantial influence on the spin distribution. Since to enumerate possible alternative magnetic configurations at each data point as we did in our preliminary calculations was infeasible, we opted to allow the magnetic moment to optimise freely in these calculations. For the same reason, we did not relax the atomic positions, although since we do not change the lengths of the

a and *b* axes in these calculations, and we would expect the in-plane bonding to be quite rigid, we expect this to be a reasonable approximation.
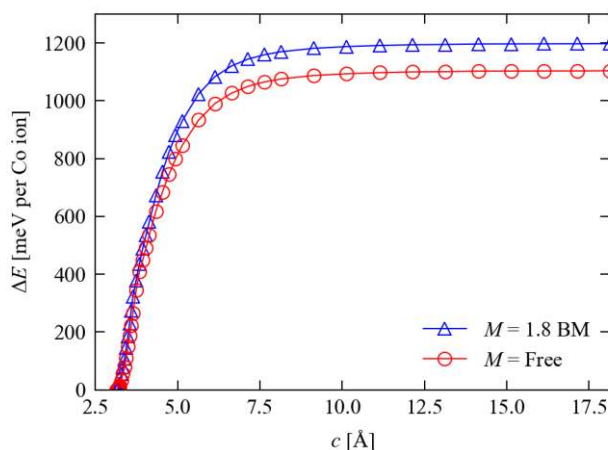

Figure S27. Energy change ΔE as a function of the interlayer spacing (*c*-axis length) of Framework **1**. Calculations were performed with the magnetic moment fixed to the lowest-energy value determined for the equilibrium structure (M = 1.8 BM per unit cell; blue tringles) and with the magnetisation allowed to freely optimise during the wavefunction minimisation (M = Free, red circles).

The change in energy as a function of the interlayer spacing is shown in Figure S27. Allowing the magnetisation to optimise freely leads to slightly lower energies as the layer separation increases, with a maximum reduction of 94 meV per Co ion (7.8 %). For interlayer spacing larger than ~9 Å the change in energy plateaus, giving interlayer interaction strengths of 1.2 /1.1 eV (116/106 kJ mol^{-1}) per Co ion with a fixed and free magnetic moment, respectively. These values are comparable to a strong hydrogen bond. Given modest amounts of thermal energy ($k_\text{B}T \approx 25$ meV at 300 K), we predict a *c*-axis expansion of approx. 0.06-0.08 Å (1.9-2.5 %) to be accessible.

The change in total energy as a function of the offset of alternate layers along the *a* and *b* axes forms a two-dimensional potential-energy surface (Figure 5 in the text; reproduced here as Figure S28). Unlike the study on the similar material Ni$_3$(HTTP)$_2$,[10] in this case we find the "eclipsed" configuration to be the energetic minimum. There appear to be local minima at layer slips of ~1.75 Å along either or both axes, albeit at ~500 meV (83 meV per Co ion) above the equilibrium structure. That the eclipsed conformation is favoured is not unexpected, since the same orbital interactions that give rise to the metallic conductivity would presumably favour this arrangement. Our analysis suggests that a small degree of misalignment should be easily accessible energetically, with sufficient thermal energy at 300 K to allow the system to explore offsets of up to 0.25 Å along either or both the two axes.
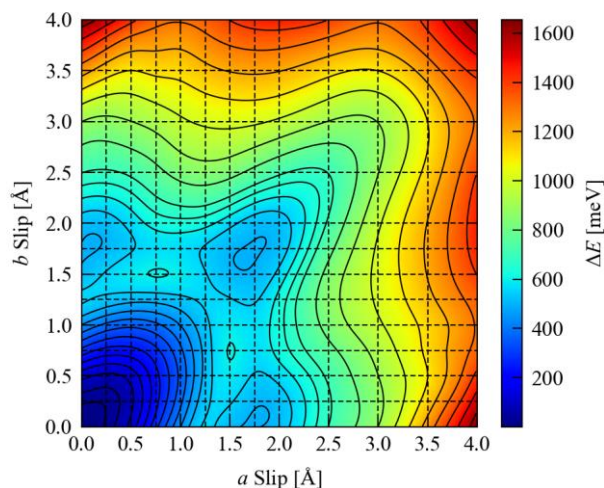
Figure S28. Contour plot of the total energy of a bilayer of Framework **1** as a function of layer offset along the crystallographic *a* and *b* axes, with the *c*-axis length optimised at each data point. A grid of calculated points, marked by dashed lines, was used to generate the smooth surface by interpolation.

Figure S29 shows the variation in the calculated electronic density of states (DoS) as the layer spacing is increased by 0.08, 0.15, 0.25 0.5 and 1 Å from the optimised equilibrium value, corresponding to energetic costs of ~26.9, 101, 236, 794 and 1608 meV per unit cell, respectively. Increasing the layer spacing causes a reduction in the density of states around the Fermi energy, with a gap opening up around 1 eV in the conduction band. A narrowing of the bandwidth is also evident, which may correspond to a reduction in the band dispersion and hence an increase in the carrier effective mass and reduced mobility.

Figure S30 shows the calculated DoS of bilayer models with layer offsets of up to 1.75 Å. Displacements of 0.25 Å along the *a*/*b* axes independently and a displacement of 0.25 Å along both axes produced a near-identical DoS, in keeping with the very similar energy evident in Figure S7, and since the lowest-energy offset appears to be the *a* = *b* line, we focussed on simultaneous offsets along both axes. Layer misalignment appears to have a similar effect to increasing the layer spacing, with a gap in the conduction band clearly evident for the 1 and 1.75 Å offsets. However, the requisite structural changes carry a much smaller energy penalty than increasing the layer separation, plus there is the possibility of local structural distortions becoming transiently "trapped" in the high-energy minima evident in Figure S7.

Taken together, these results suggest that both changes to the interlayer spacing and layer misalignment may play a role in the semimetal-to-semiconductor transition in Framework **1**, although given the significant energies associated with the larger structural distortions we would suggest that other factors, such as the behaviour of guest molecules in the pores, are likely also to play a role. One possibility is that interaction with guest molecules may shift the Fermi level, which, in combination with the opening of a gap in the conduction band, could lead to (dominant) semiconducting behaviour.
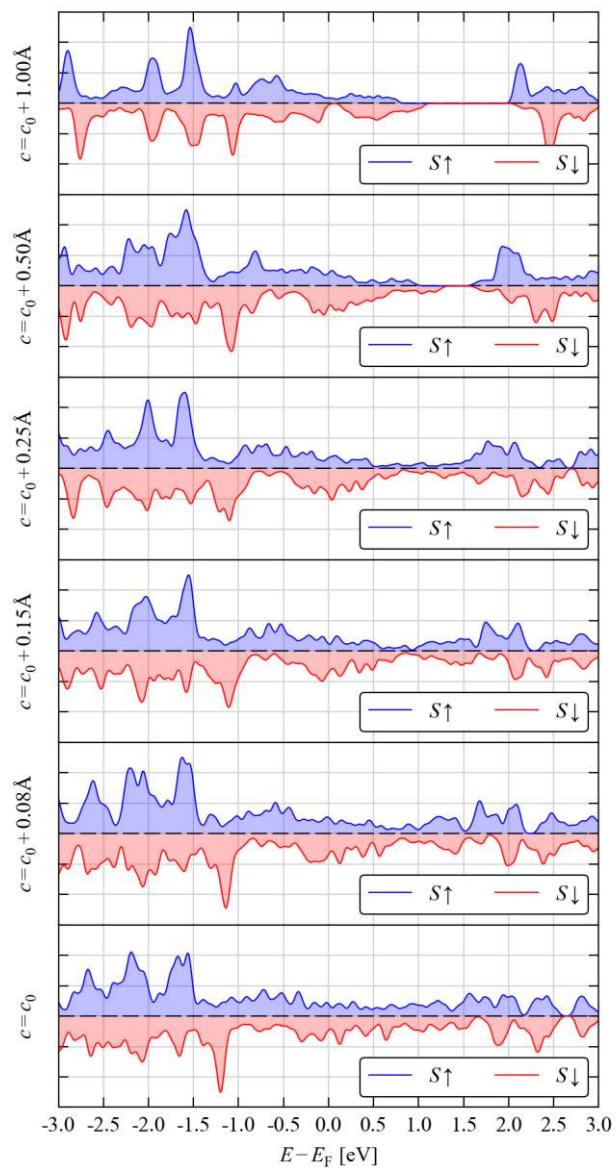
Figure S29. Calculated electronic density-of-states curves of Framework **1** with different layer spacings relative to the equilibrium value c_0. The spin-up and spin-down components of the DoS are shown as blue and red filled curves, respectively.
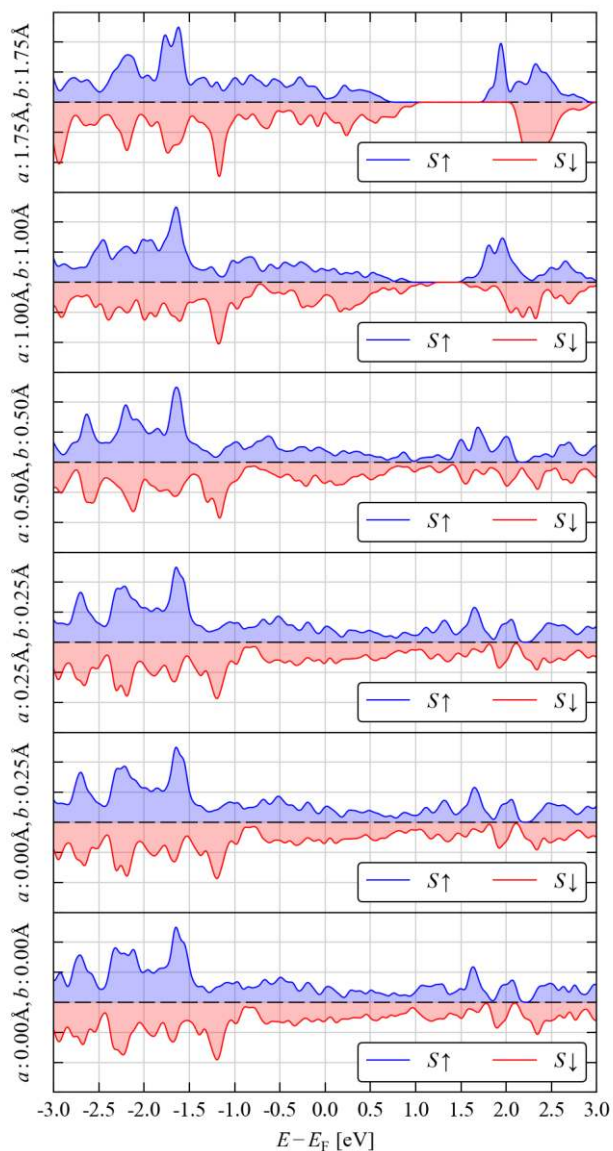
Figure S30. Calculated electronic density-of-states curves of a bilayer model of Framework **1** with several displacements of the layers along the *a* and *b* axis relative to each other. The spin-up and spin-down components of the DoS are shown as blue and red filled curves, respectively.

References:

[1] Sakamoto, R.; Kambe, T.; Tsukada, S.; Takada, K.; Hoshiko, K.; Kitagawa, Y.; Okumura, M.; Nishihara, H. *Inorg. Chem.* **2013**, *52*, 7411.

[2] Clough, A. J.; Yoo, J. W.; Mecklenburg, M. H.; Marinescu, S. C. *J. Am. Chem. Soc.* **2015**, *137*, 118.

[3] Kresse, G.; Hafner, J. *Phys. Rev. B* **1993**, *47*, 558.

[4] Perdew, J. P.; Ruzsinszky, A.; Csonka, G. I.; Vydrov, O. A.; Scuseria, G. E.; Constantin, L. A.; Zhou, X.; Burke, K. *Phys. Rev. Lett.* **2008**, *100*, 136406.

[5] Grimme, S.; Antony, J.; Ehrlich, S.; Krieg, H. *J. Chem. Phys.* **2010**, *132*, 154104.

[6] (a) Blöchl, P. E. *Phys. Rev. B* **1994**, *50*, 17953; (b) Kresse, G.; Joubert, D. *Phys. Rev. B* **1999**, *59*, 1758.

[7] Monkhorst, H. J.; Pack, J. D. *Phys. Rev. B* **1976**, *13*, 5188.

[8] Momma, K.; Izumi, F. *J. Appl. Crystallogr.* **2011**, *44*, 1272.

[9] Shojaei, F.; Hahn, J. R.; Kang, H. S. *Chem. Mater.* **2014**, *26*, 2967.

[10] Sheberla, D.; Sun, L.; Blood-Forsythe, M. A.; Er, S.; Wade, C. R.; Brozek, C. K.; Aspuru-Guzik, A.; Dincă, M. *J. Am. Chem. Soc.* **2014**, *136*, 8859.